

SPECTROMICROSCOPY OF BIOLOGICAL AND ENVIRONMENTAL SYSTEMS AT STONY BROOK: INSTRUMENTATION AND ANALYSIS

C. JACOBSEN, T. BEETZ, M. FESER, A. OSANNA,* A. STEIN and S. WIRICK
*Department of Physics & Astronomy, SUNY Stony Brook,
Stony Brook, NY 11794-3800, USA*

Soft X-ray microscopy allows one to study nanoscale heterogeneities in dry and wet environmental science, biological, polymer, and geochemical specimens. Recent advances in instrumentation at the X-1A beamline at the National Synchrotron Light Source at Brookhaven National Laboratory are described. Spectromicroscopy data analysis methods including component mapping and principal component analysis (PCA) are then discussed.

1. Introduction

Scanning transmission X-ray microscopy is used for high resolution imaging, and X-ray absorption spectroscopy of small regions. At Stony Brook, we use the method for a wide range of studies of environmental and biological systems, often in collaborations. In this paper, we outline recent advances in instrumentation and analysis methods used in these studies.

2. Microscope Instrumentation

Scanning transmission X-ray microscopes (STXMs) deliver full spatial resolution only when illuminated with a source of high spatial coherence. They are therefore well-suited to use with undulator sources at low-emittance storage rings. The X-ray ring at the National Synchrotron Light Source at Brookhaven National Laboratory has a soft X-ray undulator (X-1) that delivers quasi-monochromatic flux into a few spatial modes vertically, and about a hundred spatial modes horizontally. We have a beamline (X-1A) that delivers ~ 2 spatial modes to each of two separate microscope endstations, while allowing more than half the beam to be used by a neighboring spectroscopy beamline (X-1B). The original beamline used one monochromator with two exit slits,¹ which has since been replaced with a new pair of beamlines that

have higher energy resolution, independent monochromators for each microscope endstation.²

2.1. Zone plate optics

These scanning transmission X-ray microscopes make use of Fresnel zone plate optics to produce a high resolution focused probe. Our zone plates are fabricated using electron beam lithography in a collaborative program^{3,4} with Don Tennant of Agere Systems (formerly Lucent Technologies Bell Labs). In the past year, his laboratory has taken delivery of a JEOL JBX-9300FS electron beam lithography system. Tennant has already used this machine to draw 18 nm lines in ZEP 520 photoresist with the 100 keV beam, and he has demonstrated that the patterning accuracy is 7 nm (3σ) over a 400 μm writing field. This performance is achieved through the use of dynamic compensation of focus, stigmatism, and placement. Present efforts by A. Stein and M. Lu of Stony Brook are aimed at exploiting this system for soft X-ray zone plate fabrication; optical testing is now underway of zone plates with 160 μm diameter and 30 nm outermost zone width.

2.2. Microscope systems

The X-1A beamline has three STXMs in operation. One of these is a cryoSTXM which is used to study

*Present address: Pfarrwiesengasse 11/1/3, A-1190 Wien, Austria.

radiation-sensitive specimens at -160°C temperature. At these temperatures, radiation-induced mass loss is greatly reduced, and plunge-freezing in cryogens such as liquid ethane provides good structural preservation in biological specimens.⁵ This system has also been used for demonstrations of tomographic imaging, including a reconstruction of a frozen hydrated fibroblast at approximately $100 \times 100 \times 250$ nm resolution.⁶ Recent studies with the cryoSTXM by T. Beetz of Stony Brook have centered on a more detailed understanding of the effects of temperature on bond damage in near-edge spectroscopy.

Two new room temperature microscopes of identical design have recently entered operation.⁷ One of these is used primarily for carbon edge imaging and spectroscopy, while the other shares beamtime with the cryoSTXM and is used primarily in the 400–800 eV energy range. These microscopes have zone plate optics and order sorting apertures on kinematic mounts for easy removal and replacement, and an improved piezo stage (PI-731) with lower positional noise (< 5 nm) and significantly better field positioning (no measurable errors in ~ 30 nm resolution Michelson interferometer tests). The visible light alignment microscope, and up to two different X-ray detectors, are all mounted on a motorized platform for rapid, reproducible positioning. This has allowed us to use spatially segmented detectors in a straightforward fashion, since one can take a scan where the detector (rather than the specimen) is scanned to evaluate its properly aligned position.

2.3. Detectors

Photon counting gives the best signal-to-noise when detecting X-ray fluxes that produce signals of fewer than about 10^6 photons per second. In collaboration with G. Smith of the Instrumentation Division of the Brookhaven National Laboratory (ID-BNL), M. Feser *et al.* of Stony Brook have developed a low pressure proportional counter with essentially zero electronic noise, and a sensitivity for carbon edge X-rays limited primarily by absorption in a 100-nm-thick silicon nitride window.⁸ This detector is used for C-XANES spectromicroscopy experiments at Stony Brook.

Imaging modalities such as differential phase contrast,⁹ Nomarski differential interference contrast,¹⁰ and dark field imaging^{11–14} require the use of

a spatially configured detector. (One can also record the full microdiffraction pattern from each pixel^{15,16} at the cost of increased dataset size and image processing time.) In collaboration with P. Rehak and G. DeGeronimo (ID-BNL), and L. Strüder and P. Holl of the MPI Halbleiter (Germany), M. Feser *et al.* of Stony Brook have developed a segmented

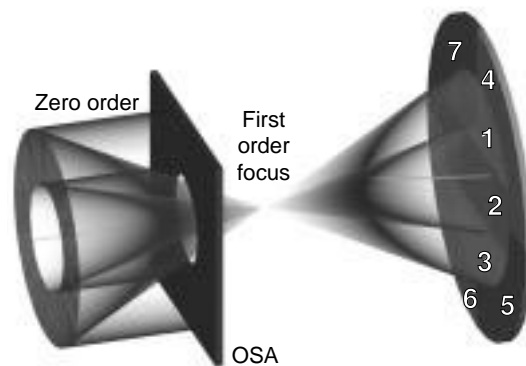


Fig. 1. Schematic view of the relationship between the focus of a zone plate in the STXM, and the segmented silicon drift detector.

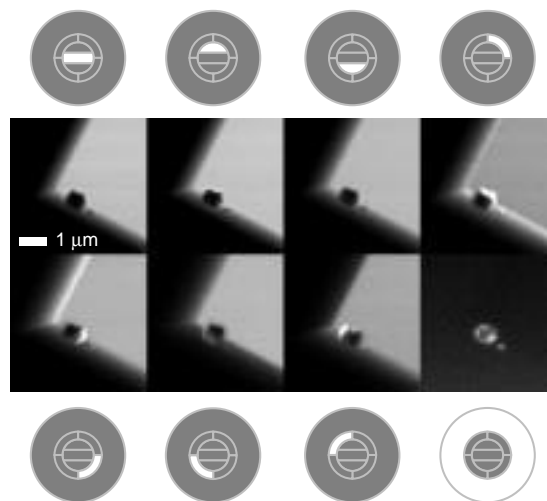


Fig. 2. Scanning transmission X-ray micrograph of a silicon nitride window corner acquired at 520 eV using a segmented silicon drift detector. Each of eight detector channels was recorded separately, all during one scan. Each image is accompanied by its corresponding detector segment, viewed from the incident beam direction. Refraction of the focused X-ray beam by the sloped wall edges of the window frame is shown in particular in the upper right and lower left images. The sharp edges of the silica dust speck located near the window corner are particularly well highlighted by the outermost detector segment which yields a darkfield image.

silicon drift detector (see Fig. 1) with low noise read-out electronics.⁷ This detector operates at room temperature without any entrance window, and has a noise equivalent of about five photons per pixel at 1 millisecond dwell time. An example of the information this detector delivers is shown in Fig. 2, illustrating the phase advance X-ray beams experience in solids.¹⁷

3. Spectromicroscopy Analysis

Soft X-ray transmission microscopes can combine high spatial resolution imaging with high energy resolution absorption spectroscopy.^{18,19} These capabilities are used for a number of investigations in environmental science, biology, geochemistry, polymer science, and other fields. We wish to discuss here some methods that can be used for analysis of these specimens.

In the X-ray microscope, we obtain images (maps of transmitted flux I) according to the Lambert–Beer law for absorption:

$$I = I_0 \exp(-\mu t), \quad (1)$$

where I_0 is the incident X-ray flux, μ is a linear absorption coefficient for a specific material, and t is the thickness of that material. In fact, the absorption coefficient $\mu(E)$ is photon-energy-dependent, with a general $\sim 1/E^3$ dependence on photon energy E , and steplike changes on either side of X-ray absorption edges. The soft X-ray absorption coefficients $\mu(E)$ for all elements are well known and tabulated²⁰ at photon energies more than about 30 eV away from absorption edges, so one can use μ/ρ to obtain quantitative measurements of the mass per unit area ρt of an element from images obtained at absorption edges.^{21,22}

Beyond elemental mapping, one can also obtain chemical state sensitivity by using XANES resonances near absorption edges. For a thickness t of a single material, a measurement of the transmitted flux $I(E)$ relative to the incident flux $I_0(E)$ provides a means to calculate the energy-dependent optical density:

$$D(E) = -\ln\left(\frac{I(E)}{I_0(E)}\right) = \mu(E)t. \quad (2)$$

If, however, we measure the optical density not over a continuous energy range E but at some set of $n = 1$ K N discrete energies E_n , we then measure

$$D_n = \mu_n t \quad (3)$$

for each of the $n = 1$ K N photon energies. Let us next consider a mixture of $s = 1$ K S different materials; our total measurement of optical density D_n at one-photon energy is given by the combined absorption of all the materials, or

$$D_n = \mu_{n1}t_1 + \mu_{n2}t_2 + K + \mu_{nS}t_S. \quad (4)$$

Finally, if we carry out this measurement not from a single homogeneous mixture but from heterogeneous pixels $p = 1$ K P indexed by $p = i_{\text{column}} + (i_{\text{row}} - 1) \cdot (\#\text{columns})$ in an image, the optical density measured at one pixel p is given by

$$D_{np} = \mu_{n1}t_{1p} + \mu_{n2}t_{2p} + K + \mu_{nS}t_{Sp}. \quad (5)$$

When all N photon energies are considered, we see that we have a data matrix D_{NP} of

$$\begin{bmatrix} D_{11} & K & D_{1P} \\ M & O & K \\ D_{N1} & \Lambda & D_{NP} \end{bmatrix} = \begin{bmatrix} \mu_{11} & \Lambda & \mu_{1S} \\ M & O & M \\ \mu_{N1} & \Lambda & \mu_{NS} \end{bmatrix} \cdot \begin{bmatrix} t_{11} & \Lambda & t_{1P} \\ M & O & M \\ t_{S1} & \Lambda & t_{SP} \end{bmatrix} \quad (6)$$

or $D_{N \times P} = \mu_{N \times S} \cdot t_{S \times P}$.

3.1. Mapping from known spectra

A common mode of operation for the X-1A microscopes is to take a series of images at different photon energies. Due to deviations from perfect straight-line motion in the translation stages used to compensate for changes in zone plate focal length with photon energy, these images must then be aligned to each other to yield a “stack” of spectrum image data²³ in position and energy, or (x, y, E) . When we acquire such a series of images at different photon energies N , we are in fact measuring the data matrix $D_{N \times P}$. If we know the exact absorption spectrum μ_{NS} for each of the $s = 1$ K S components in the sample, then we can find the spatially resolved thicknesses of the components by matrix inversion:

$$t_{S \times P} = \mu_{S \times N}^{-1} \cdot D_{N \times P}. \quad (7)$$

The inversion of the matrix $\mu_{N \times S}$ can be accomplished in a robust fashion using singular value decomposition (see e.g. Ref. 24). This method for composition mapping was first applied to X-ray microscopy by Zhang in work with Balhorn *et al.* on measuring protein and DNA concentrations in animal sperm.²⁵ In that work, images at $N = 6$ different photon energies were individually acquired at energies between 281.8 and 302.4 eV. In this earlier work, the images were aligned to each other “by hand,” by observing the difference signal between two images and adjusting an (x, y) shift to minimize its appearance. This procedure yielded a data matrix $D_{N \times P}$, and measurements of the absorption spectra of a thin film standard of DNA and of bovine serum albumin (as a representative protein) made it possible to obtain quantitative maps of the matrix $t_{S \times P}$ for $S = 2$ components over $P \approx 40,000$ pixels. Similar procedures have since been used by a number of investigators.

To obtain quantitatively accurate components maps $t_{S \times P} = \mu_{S \times N}^{-1} \cdot D_{N \times P}$ we must make sure that the data matrix $D_{N \times P}$ is free from significant errors. For this to be true, we must work hard to minimize second harmonic contamination from the monochromator. When the X-1A beamline monochromator is tuned to 300.0 eV, some 600.0 eV light is also present at the exit slit. An imperfectly absorbing central stop (see Fig. 1) will allow some of this 600 eV light to reach the specimen plane. Furthermore, if the zone plate has a line:space ratio other than exactly 1:1, it will exhibit some second diffraction order focusing and this will be coincident with the first diffracted order focus. These effects would produce a weakly absorbed signal generating twice as much ionization in our detector, and would cause us to overestimate X-ray transmission and thereby underestimate X-ray optical density D at XANES resonance peak energies (see e.g. Ref. 26). Our approach to filtering out the 600 eV contribution is to make the X-ray beam reflect off of two fused quartz mirrors at about 40 mrad grazing incidence angle each.² However, the surface roughness of these mirrors should be very small compared to the $\lambda = 2-4$ nm X-ray wavelengths we use. This requires careful, stress-free mounting (so as to avoid mirror curvature which would otherwise produce aberrations affecting the coherence of the zone plate illumination) of highly polished mirrors. An ultrahigh vacuum chamber and mirror positioning

system for this purpose has been designed by M. Carlucci-Dayton *et al.* of Stony Brook,²⁷ and this improved order sorting apparatus has been installed for one of the two microscope endstations.

3.2. Principal component analysis

With automated data collection and alignment, we now often have data sets $D_{N \times P}$ at $N = 100-150$ photon energies with $P > 100,000$ pixels. Especially when “natural” specimens such as those encountered in environmental science or biology are studied, we may not know ahead of time the spectra $\mu_{S \times N}^{-1}$ of all S components in the specimen, leaving us unable to determine component thicknesses from $t_{S \times P} = \mu_{S \times N}^{-1} \cdot D_{N \times P}$. Fortunately, more powerful methods of spectroscopic data analysis exist. Principal component analysis was first developed in the social sciences decades ago, but it has proven to be very powerful in chemical analysis (see e.g. Ref. 28). It has also been used for spectrum imaging in electron microscopes equipped with energy loss spectrometers,^{29,30} and its use in X-ray microscopy has been explored by P. King *et al.*,^{31,32} A. Hitchcock of McMaster University, and A. Osanna *et al.* of Stony Brook.^{33,34}

Principal component analysis is based on examination of the covariance matrix $Z_{N \times N} = D_{N \times P} \cdot D_{P \times N}^T$ formed from the data matrix $D_{N \times P}$ and its transpose. The covariance matrix $Z_{N \times N}$ therefore measures the correlations between images at various energies, and because the correlation of the image at energy n_1 with n_2 is the same as the correlation of n_2 with n_1 , the covariance matrix $Z_{N \times N}$ is symmetric. Assuming that we will find S_{abstract} distinguishable components, we then wish to find the $s = 1$ K S eigenvalues $\lambda(s)$ and eigenvectors $r(s)_{N \times 1}$ which characterize the covariance matrix:

$$Z_{N \times N} \cdot r(s)_{N \times 1} = \lambda(s)r(s)_{N \times 1}. \quad (8)$$

The eigenvectors $r(s)_N$ each have N points, just like absorption spectra $\mu_{N \times S}$, so we will call them eigenspectra. If we sort the results in order of decreasing magnitude of the corresponding eigenvalues $\lambda(s)$, we then form an eigenspectra matrix

$$C_{N \times S_{\text{abstract}}} = \begin{bmatrix} r(1)_1 & \Lambda & r(S_{\text{abstract}})_1 \\ \text{M} & \text{O} & \text{M} \\ r(1)_N & \Lambda & r(S_{\text{abstract}})_N \end{bmatrix} \quad (9)$$

where the leftmost column contains the principal eigenspectrum (the spectrum that is most in common with all the spectra from all the pixels in the data matrix $D_{N \times P}$). We therefore find that a column matrix $C_{N \times S_{\text{abstract}}}$ is calculated directly from the data with no assumptions made about what the abstract components $s = 1 \text{ K } S_{\text{abstract}}$ are.

Once the column matrix $C_{N \times S_{\text{abstract}}}$ of eigenspectra has been calculated, we can also obtain eigenimages associated with each of these spectra. Our expectation is that the data matrix is the result of $D_{N \times P} = \mu_{N \times S} \cdot t_{S \times P}$, where S refers to actual components with spectra $\mu_{N \times S}$ and thicknesses $t_{S \times P}$. Our solution $C_{N \times S_{\text{abstract}}}$ gives us eigenspectra corresponding to abstract components S_{abstract} , and we therefore expect to find eigenimages $R_{S_{\text{abstract}} \times P}$ associated with our data matrix:

$$D_{N \times P} = C_{N \times S_{\text{abstract}}} \cdot R_{S_{\text{abstract}} \times P}. \quad (10)$$

Because the eigenspectra $C_{N \times S_{\text{abstract}}}$ are orthogonal, the inverse of $C_{N \times S_{\text{abstract}}}$ is just its transpose, and so we can obtain the eigenimages from

$$R_{S_{\text{abstract}} \times P} = C_{S_{\text{abstract}} \times N}^T \cdot D_{N \times P}. \quad (11)$$

We now consider an example of principal component analysis. Milk is a biological colloid consisting of about 85% water, 5% lactose, 4% lipids, 3% of various proteins (primarily casein), and other components. Following data set alignment and normalization, eigenspectra $C_{N \times S_{\text{abstract}}}$ were calculated in about a minute's time using the standard eigenvector solution routine available in the software package IDL (Research Systems Inc.) on a Pentium/Linux computer. In Fig. 3, the first 30 eigenvalues are shown of a carbon-XANES milk data set $D_{N \times P}$ with $N = 200$, acquired from a few-micrometer-thick milk layer sandwiched between two 100-nm-thick silicon nitride windows.³⁵ The first eigenspectrum looks very much like a typical carbon XANES absorption spectrum, and in some sense it represents an average of all the different spectra contained in the data set $D_{N \times P}$. The second eigenspectrum represents the most dominant difference from the average, and subsequent eigenspectra give successive spectral differences. As can be seen

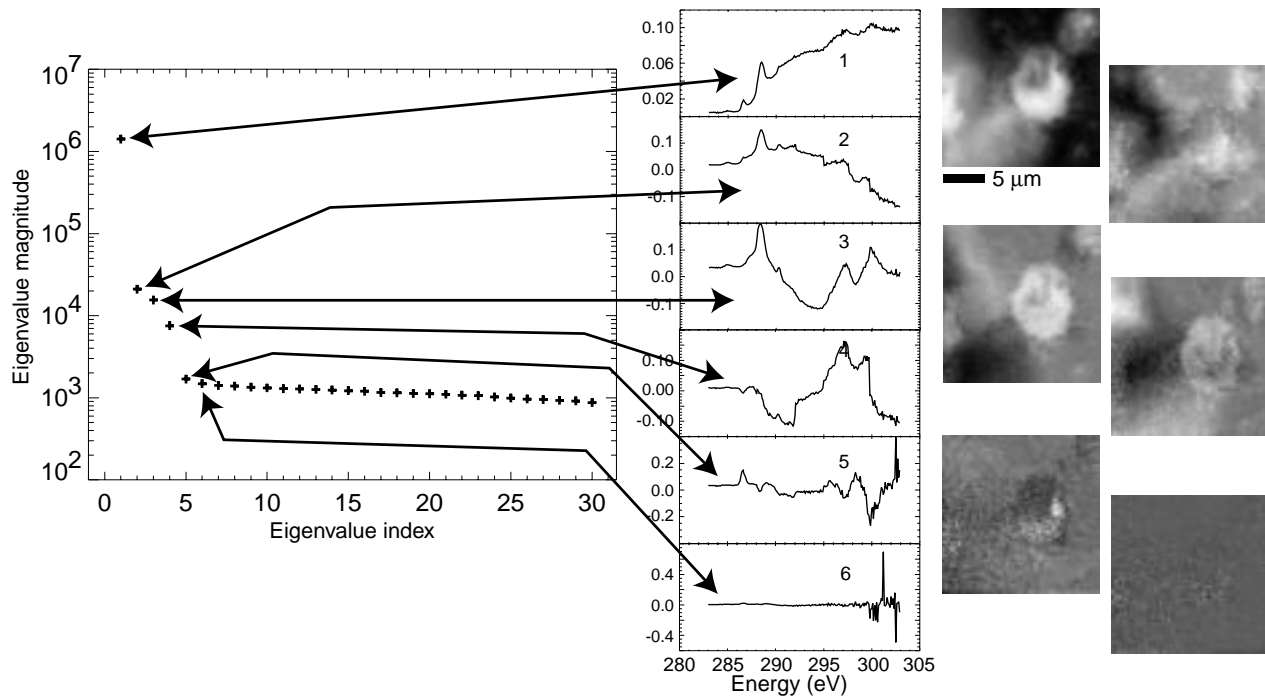


Fig. 3. An example of principal component analysis on a lipid droplet in milk. The first 30 of 200 eigenvalues are shown in the plot at left. As can be seen, the eigenvalues (and therefore the weighting of the corresponding eigenspectra, which are shown in the middle) drop rapidly for components $s = 1-5$, until component $s = 6$ simply shows noise in the sixth eigenspectrum and eigenimage. Data acquired by S. Abend; similar data have also been obtained at X-1A by U. Neuhausler (both at Stony Brook at that time).

in Fig. 3, the eigenvalues decline quickly from $s = 1$ to $s = 5$, so that by the time we get to $s = 6$ and beyond the eigenspectra and eigenimages simply reflect nonsignificant variations in photon statistics noise in the data set $D_{N \times P}$. We can therefore limit the eigenspectra and eigenimage solutions to $S_{\text{abstract}} = 5$ components in this case, and we call these our principal components.

Because the eigenspectra are orthogonal, we can represent the spectrum at any point in the data matrix $D_{N \times P}$ with some linear combination of eigenspectra $C_{N \times S_{\text{abstract}}}$. To do this, we must find a transformation matrix between eigenspectra $C_{N \times S_{\text{abstract}}}$, and the spectra of actual components $\mu_{N \times S}$. This transformation (a rotation in multidimensional space) is given by

$$T_{S_{\text{abstract}} \times S} = C_{S_{\text{abstract}} \times N}^T \cdot \mu_{N \times S}. \quad (12)$$

With this transformation matrix, we can map the eigenspectra $C_{N \times S_{\text{abstract}}}$ onto the observed spectra with

$$\mu_{N \times S} = C_{N \times S_{\text{abstract}}} \cdot T_{S_{\text{abstract}} \times S}, \quad (13)$$

and we can calculate actual component thickness maps $t_{S \times P}$ using

$$t_{S \times P} = T_{S \times S_{\text{abstract}}}^{-1} \cdot C_{S_{\text{abstract}} \times N}^T \cdot D_{N \times P}. \quad (14)$$

However, we see that this method requires us to know all of our actual component spectra $\mu_{N \times S}$ from the outset, whereas if this were indeed the case we might simply obtain thickness maps from $t_{S \times P} = \mu_{S \times N}^{-1} \cdot D_{N \times P}$. The power of PCA is that because the eigenspectra are calculated *without* advance knowledge of all that is in the specimen, we can obtain information about additional spectromicroscopic components in a data set $D_{N \times P}$ starting from *incomplete* knowledge about the specimen. While we have only begun to develop a procedure appropriate for X-ray microscopy data sets, approaches appropriate for other types of data are well established.²⁸ A variation of partial least squares (PLS) regression^{28,36} might involve using known spectra to define an initial basis set, and then calculating subsequent eigenspectra corresponding to the most significant components other than those that are known. In this approach, eigenspectra are found one at a time and

the covariance matrix $Z_{N \times N}$ is subsequently reduced before the next eigenspectrum is found.

4. Conclusion

Soft X-ray spectromicroscopy provides a new set of tools for nanometer scale characterization of chemical heterogeneities. This is being used in environmental science, polymer research, biology, and geochemistry, among other fields. At present, most efforts in quantitative chemical state mapping have concentrated on systems where spectra can be obtained from purified versions of all the specimen's components. Especially with natural specimens, all components may not be known ahead of time, but methods such as principal component analysis may provide the right sort of tools to separate unknown from known components as a first step towards their subsequent identification based on location and/or spectral signatures.

Acknowledgments

We wish to thank Adam Hitchcock and Steve Wasserman for helpful discussions. Work supported by the National Science Foundation under grants DBI-9986819 and ECS-0099893.

References

1. H. Rarback *et al.*, *Journal of X-Ray Science and Technology* **2**, 274 (1990).
2. B. Winn *et al.*, *Journal of Synchrotron Radiation* **7**, 395 (2000).
3. S. Spector, C. Jacobsen and D. Tennant, *Journal of Vacuum Science and Technology* **B15**(6), 2872 (1997).
4. D. Tennant *et al.*, in *X-Ray Microscopy: Proc. Sixth International Conference*, eds. W. Meyer-Ilse, A. Warwick and D. T. Attwood (American Institute of Physics, New York, 2000), pp. 601–6.
5. J. Maser *et al.*, *Journal of Microscopy* **197**, 68 (2000).
6. Y. Wang *et al.*, *Journal of Microscopy* **197**, 80 (2000).
7. M. Feser *et al.*, in *X-Ray Microscopy: Proc. Sixth International Conference*, eds. W. Meyer-Ilse, A. Warwick and D. T. Attwood (American Institute of Physics, New York, 2000), pp. 367–72.
8. M. Feser *et al.*, *SPIE* **3449**, 19 (1998).
9. J. R. Palmer and G. R. Morrison, in *X-Ray Microscopy III*, eds. A. G. Michette, G. R. Morrison and C. J. Buckley (Springer-Verlag, Berlin, 1992), pp. 278–80.
10. F. Polack *et al.*, in *X-Ray Microscopy: Proc. Sixth*

- International Conference*, eds. W. Meyer-Ilse, A. Warwick and D. T. Attwood (American Institute of Physics, New York, 2000), pp. 573–80.
11. G. R. Morrison and M. T. Browne, *Review of Scientific Instruments* **63**, 611 (1992).
 12. H. N. Chapman, C. Jacobsen and S. Williams, *Ultramicroscopy* **62**(3), 191 (1996).
 13. H. N. Chapman *et al.*, *Journal of the Microscopy Society of America* **2**(2), 53 (1996).
 14. S. Vogt *et al.*, *Ultramicroscopy* **87**, 25 (2001).
 15. G. R. Morrison, in *X-Ray Microscopy IV* (Chernogolovka, Russia, Bogorodskii Pechatnik, 1994).
 16. H. N. Chapman, *Ultramicroscopy* **66**, 153 (1996).
 17. G. Kellström, *Nova Acta Regiae Societatis Scientiarum Upsaliensis* **8**, 1 (1932).
 18. H. Ade *et al.*, *Science* **258**, 972 (1992).
 19. X. Zhang *et al.*, *Nucl. Instrum. Methods Phys. Res.* **A347**, 431 (1994).
 20. B. L. Henke, E. M. Gullikson and J. C. Davis, *Atomic Data and Nuclear Data Tables* **54**, 181 (1993).
 21. A. Engström, *Acta Radiologica (Supplementum LXIII)* **63**, 1 (1946).
 22. E. Bigler, F. Polack and S. Lowenthal, *Optics Communications* **41**, 6 (1982).
 23. C. Jacobsen *et al.*, *Journal of Microscopy* **197**, 173 (2000).
 24. W. H. Press *et al.*, *Numerical Recipes in Fortran 77: The Art of Scientific Computing* (Cambridge University Press, 1986).
 25. X. Zhang *et al.*, *Journal of Structural Biology* **116**, 335 (1996).
 26. C. J. Buckley, in *X-Ray Microscopy: Proc. Sixth International Conference*, eds. W. Meyer-Ilse, T. Warwick and D. Attwood (American Institute of Physics, New York, 2000), pp. 33–40.
 27. M. Carlucci-Dayton, in *Department of Physics and Astronomy* (State University of New York at Stony Brook: Stony Brook, New York, 2000), p. 155.
 28. E. R. Malinowski, *Factor Analysis in Chemistry*, 2nd edition, ed. (John H. Wiley & Sons, New York, 1991).
 29. N. Bonnet *et al.*, *Ultramicroscopy* **40**, 1 (1992).
 30. N. Bonnet, N. Brun and C. Colliex, *Ultramicroscopy* **77**, 97 (1999).
 31. P. L. King *et al.*, *Nucl. Instrum. Methods Phys. Res.* **A291**, 19 (1990).
 32. P. L. King *et al.*, *J. Vac. Sci. Tech.* **A7**(6), 3301 (1989).
 33. A. Osanna and C. Jacobsen, in *X-Ray Microscopy: Proc. Sixth International Conference*, eds. W. Meyer-Ilse, T. Warwick and D. T. Attwood (American Institute of Physics, New York, 2000), pp. 350–7.
 34. A. Osanna, in *Department of Physics and Astronomy* (State University of New York at Stony Brook: Stony Brook, New York, 2000), p. 150.
 35. U. Neuhäusler *et al.*, *Journal of Synchrotron Radiation* **7**, 110 (2000).
 36. P. Geladi and B. R. Kowalski, *Analytica Chimica Acta* **185**, 1 (1986).